Aalborg Universitet

AALBORG UNIVERSITY
DENMARK

Robust Two Degrees-of-freedom Single-current Control Strategy for LCL-type Grid-Connected DG System under Grid-Frequency Fluctuation and Grid-impedance Variation

Zhou, Leming; Chen, Yandong; Luo, An; Guerrero, Josep M.; Zhou, Xiaoping; Chen, Zhiyong; Wu, Wenhua

Published in:
IET Power Electronics

DOI (link to publication from Publisher):
10.1049/iet-pel.2016.0120

Publication date:
2016

Document Version
Early version, also known as pre-print

Link to publication from Aalborg University

Citation for published version (APA):
Zhou, L., Chen, Y., Luo, A., Guerrero, J. M., Zhou, X., Chen, Z., & Wu, W. (2016). Robust Two Degrees-of-freedom Single-current Control Strategy for LCL-type Grid-Connected DG System under Grid-Frequency Fluctuation and Grid-impedance Variation. *IET Power Electronics*, *9*(14), 2682 - 2691. https://doi.org/10.1049/iet-pel.2016.0120

General rights
Copyright and moral rights for the publications made accessible in the public portal are retained by the authors and/or other copyright owners and it is a condition of accessing publications that users recognise and abide by the legal requirements associated with these rights.

- Users may download and print one copy of any publication from the public portal for the purpose of private study or research.
- You may not further distribute the material or use it for any profit-making activity or commercial gain
- You may freely distribute the URL identifying the publication in the public portal -

Robust Two Degrees-of-freedom Single-current Control Strategy for LCL-type Grid-Connected DG System under Grid-Frequency Fluctuation and Grid-impedance Variation

Leming Zhou[1], Yandong Chen[1*], An Luo[1], Josep M. Guerrero[2], Xiaoping Zhou[1], Zhiyong Chen[1], and Wenhua Wu[1]

1. College of Electrical and Information Engineering, Hunan University, Changsha, China

2. Department of Energy Technology, Aalborg University, Aalborg East 9220, Denmark

[*]yandong_chen@hnu.edu.cn

***Abstract*—For LCL-type grid-connected distributed generation (DG) system, the grid-frequency fluctuation and grid-impedance variation affect the active/reactive power control accuracy and resonance peak suppression respectively, which would reduce the system robustness. In this paper, a robust two degrees-of-freedom single-current control (RTDOF-SCC) strategy is proposed, which mainly includes the synchronous reference frame quasi-proportional-integral (SRFQPI) control and robust grid-current-feedback active damping (RGCFAD) control. The proposed SRFQPI control can compensate the local-loads reactive power, and regulate the instantaneous grid current without steady-state error regardless of the fundamental frequency fluctuation. Simultaneously, the proposed RGCFAD control effectively damps the LCL-resonance peak regardless of the grid-impedance variation, and further improves both transient and steady-state performances. The stability margin and dynamic response of the overall system are analyzed in detail, and the proper parameters are selected without complicated trial. Finally, Simulation and experimental results verify the proposed control and design strategies.**

***Index Terms*—Grid-connected inverter, LCL-filter, two degrees-of-freedom, single-current control, active damping**

1. INTRODUCTION

With the shortage of fossil energy and deterioration of environmental pollution, renewable energy (e.g. wind and solar energy) distributed generations (DGs) have been attracted more attention, and have become a research hotspot [1]. As a key interface between DGs and utility grid, LCL-type grid-connected inverter has become a popular and cost-effective application. However, there are still some unsolved problems for LCL-type inverter as follows: i) Since the DGs are widely installed at the end of the feeder, it is necessary to compensate the load reactive power in order to remain the feeder steady [2]; ii) Since LCL-filter is a three-order low-damping system, it easily occurs to resonance, and then affects the system stability [3]; iii) Since plenty of DGs and local loads are injected into the utility grid, the influences of grid-frequency fluctuation and grid-impedance variation can not be negligible for the LCL-type grid-connected inverter [4]. Especially, the grid-frequency fluctuation affects active/reactive

power control [5], and the grid-impedance variation affects the LCL-resonance suppress [6]. These problems are urgent to be considered and solved in the DGs.

To regulate active and reactive powers, the synchronous reference frame (SRF) theory and the instantaneous reactive power (IRP) theory are the most addressed ones for the three-phase system [7-8]. Through creating an orthogonal imaginary variable from an original single-phase signal, active and reactive powers can also be conveniently regulated by using SRF and IRP techniques for the single-phase system [9]. Using a conventional SRF proportional- integral (SRFPI) regulator, the DGs can easily achieve zero steady-state error. Thus, the SRFPI regulator is considered to be superior to the PI regulator in the stationary coordinate frame [10]. However, the system stability and total harmonic distortion (THD) are greatly influenced by the grid-frequency fluctuation and grid-voltage distortion since the SRFPI regulator depends extremely on the synchronous reference frame phase-locked loop (SRF-PLL) [5]. Therefore, it is necessary to improve the robustness of SRF control system against grid-frequency fluctuation.

To damp the LCL-resonance peak, active damping methods for the LCL-type grid-connected inverter have been discussed, mainly including the capacitor-voltage feedback (CVF) [11], capacitor-current feedback (CCF) [12], multivariable composite feedback (MCF) [13], grid-current feedback (GCF) [14-15], and so on. Compared with the extra-feedback methods, the GCF active damping method does not demand an additional sensor or a complex software-based observer, which can reduce the complexity as well as improve the reliability in the practical cases. Especially, the GCFAD method with high-pass-filter (HPF) has drawn much attention for its simple implementation and no noise disturbance [14-15]. However, the impact of grid-impedance variation on the GCF active damping methods is unconsidered in the digital control. Since the control delay derived from the digital controller can drift the virtual equivalent damping resistance (VEDR) from its designed value [16], the control system stability is always drastically deteriorated. For instance, when the LCL-resonance frequency shifts to one-sixth of switching frequency f_s due to the potential influence of the grid impedance, the VEDR of CCF active damping method equals to zero at the LCL-resonance frequency [12]. Consequently, the DGs can be hardly stable no matter how much the CCF coefficient is selected. Also, the similar phenomenon will occur in the GCF active damping method since its critical frequency is located in the range of LCL-resonance frequency [15]. To enhance the system damping and stability, the LCL-resonance frequency must keep away from the critical frequency which causes the VEDR equals to zero [17]. However, the LCL-resonance frequency always occurs shifting with the grid-impedance variation since the transmission lines and isolation transformers should not be negligible [18-19]. Consequently, the potential instability will be triggered if the grid-impedance variation imposes the LCL-resonance frequency migrating to the critical frequency. It is necessary to improve the robustness of the control system in case of grid-impedance variation.

In this paper, a robust two degrees-of-freedom single-current control (RTDOF-SCC) strategy is proposed for single-phase LCL-type grid-connected DG System, which mainly includes the synchronous reference frame quasi-proportional–integral (SRFQPI) controller and robust grid-current-feedback active damping (RGCFAD) controller. The paper is organized as follows. The configuration and control strategy of photovoltaic (PV) DG system is described in Section 2. In Section 3, the performance of the RGCFAD controller is analyzed, and its optimized parameters are selected. The dynamic response and stability margin of the overall system are analyzed in detail, and the proper parameters of RTDOF-SCC are selected. Simulation and experimental results are illustrated in Section 4. Some conclusions are given in Section 5.

2. SYSTEM MODELING AND CONTROL METHOD

The structure of single-phase LCL-type grid-connected PV system is shown in Fig. 1, which mainly includes PV arrays, main circuits, local loads and control circuits. The main circuits are composed of the boost circuit, the single-phase full-bridge inverter, and the LCL-filter. The boost circuit transfers solar energy from PV arrays to the dc-link energy-storage capacitor C_{dc} through the maximum-power-point-tracking (MPPT) control [3]. The single-phase full-bridge inverter transmits the energy into the grid and local loads through the proposed RTFOF-SCC control. L_g is the grid inductance. L_1 and L_2 are the inverter-side and grid-side LCL-filter inductances, respectively, and their equivalent series resistances are R_1 and R_2. C is the LCL-filter capacitance. u_{dc} is the dc-link voltage, and u_{inv} is the inverter output voltage. u_{pcc} is the point of common coupling voltage. u_s is the grid voltage. i_g is the grid current, and i_s is the true injected grid current.

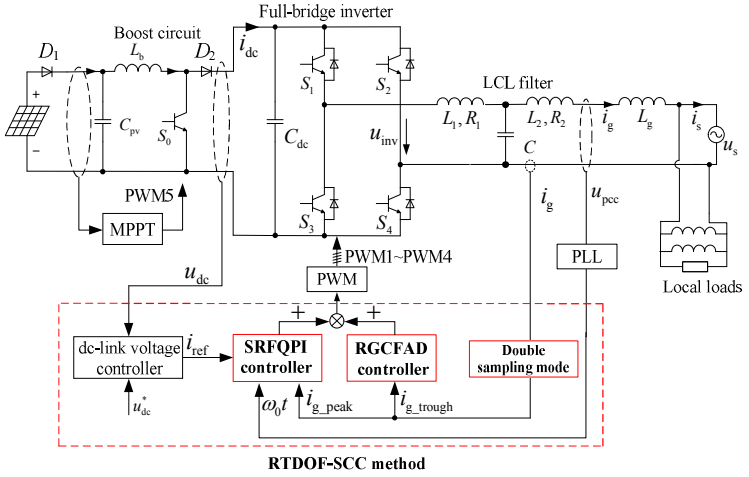

Fig.1. Configuration of single-phase LCL-type grid-connected PV system.

As shown in Fig. 2 (a), the proposed RTDOF-SCC control strategy is composed of the dc-link voltage controller, double-sampling mode, the SRFQPI controller and RGCFAD controller. The outer dc-link voltage controller keeps the dc-link voltage steady in the reference voltage u_{dc}^* [1]. The double-sampling mode reduces the control delay of active-damping loop through sampling the grid-current signal twice in each switching period T_s. The SRFQPI controller compensates reactive power quickly

and regulates the instantaneous grid current without steady-state error regardless of the grid-frequency fluctuation. The RGCFAD controller damps LCL-resonance peak and improves the system robustness against the grid-impedance variation. ω_0 is the fundamental angular frequency. K_{inv} is the inverter gain. I_{p}^* and I_{q}^* are the active and reactive reference currents, respectively [3]. $G_{\text{h}}(s)$ is the transfer function of Zero-Order-Holder (ZOH). λ_1 and λ_2 are the computation delay coefficients of SRFQPI and RGCFAD, respectively. $G_{\text{control1}}(s)$ and $G_{\text{control2}}(s)$ are the transfer functions of SRFQPI and RGCFAD control delays, respectively, and expressed as Eq.(1) [18].

$$G_{\text{control}i}(s) = e^{-\lambda_i s T_{\text{s}}} G_{\text{h}}(s) / T_{\text{s}}, \quad 0 \le \lambda_i \le 1, \ i = 1,2 \tag{1}$$

where,

$$G_{\text{h}}(s) = \frac{1 - e^{-sT_{\text{s}}}}{s} \tag{2}$$

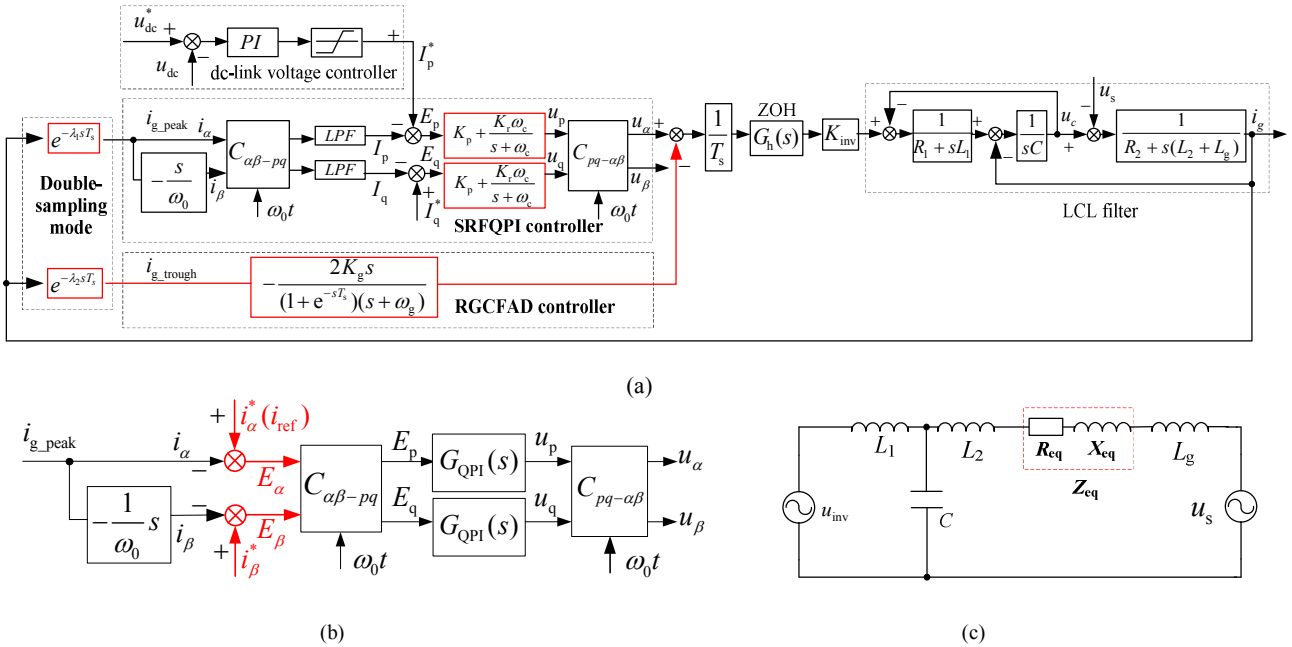

(a)

(b)

(c)

Fig. 2. Block diagram of the proposed RTDOF-SCC method and equivalent mode. (a) The proposed RTDOF-SCC method. (b) Equivalent structure of the proposed SRFQPI controller. (c) Equivalent electrical mode after introducing virtual impedance of RGCFAD controller.

In the double-sampling mode, the sampling instants of i_g are located at the peak and trough of the triangular carrier wave to avoid introducing the switching ripples. The two sampling values $i_{\text{g\_peak}}$ and $i_{\text{g\_trough}}$ are set as the input signals of SRFQPI and RGCFAD, respectively. In this mode, λ_1=1 and λ_2=0.5, so it can reduce the control delay of the active-damping loop as well as minimize the influence of the control delay on the VEDR.

Meanwhile, the transfer function $G_{\text{LCL}}(s)$ from i_{g} to u_{inv} can be derived as follows.

$$G_{\text{LCL}}(s) = \frac{i_{\text{g}}(s)}{u_{\text{inv}}(s)} = \frac{1}{s(s^2 + \omega_{\text{res}}^2)} \tag{3}$$

where ω_{res} is the LCL-resonance angular frequency, expressed as Eq. (4).

$$\omega_{\text{res}} = \sqrt{\frac{L_1 + L_2 + L_g}{L_1(L_2 + L_g)C}} \tag{4}$$

2.1. SRFQPI controller

To regulate active and reactive powers, the grid current i_g is transformed in the synchronous-reference frame as shown in Fig.2 (a). Using the derivative of the α-phase grid current i_{g_peak}[3], the virtual β-phase current is obtained to construct the orthogonal two-phase currents for detecting the reactive current quickly in the stationary coordinate frame. To reduce the effect of grid-frequency offset, the quasi-proportional–integral (QPI) controller is proposed in the *d-q* rotating coordinate frame for obtaining a SRFQPI controller in the α-β stationary coordinate frame, which is equivalent to the characteristics of QPR controller.

Assuming $i_\alpha = i_{g\_peak}$, the virtual β-phase current i_β can be obtained by the derivative of $i_{g\_peak}(s)$, and i_β can be expressed as follows.

$$i_\beta(s) = -\frac{s}{\omega_0} i_{g\_peak}(s) \tag{5}$$

Then, the dc components of active current I_p and reactive current I_q are derived as follows.

$$\begin{bmatrix} I_p \\ I_q \end{bmatrix} = \begin{bmatrix} \sqrt{2} I_g \cos\theta \\ \sqrt{2} I_g \sin\theta \end{bmatrix} \tag{6}$$

where I_g is the RMS value of grid-current i_g at the fundamental frequency ω_0, and θ is the initial phase-angle difference between grid-current component and grid-voltage component at ω_0.

The QPI regulator is proposed to control the active and reactive current errors E_p, E_q accurately, expressed as Eq. (7).

$$\begin{cases} u_p(s) = G_{QPI}(s) E_p = G_{QPI}(s)(I_p^* - I_p) \\ u_q(s) = G_{QPI}(s) E_p = G_{QPI}(s)(I_q^* - I_q) \end{cases} \tag{7}$$

where u_p and u_q are the output signals values of $G_{QPI}(s)$ in the *d-q* rotating coordinate. The transfer function of $G_{QPI}(s)$ is expressed as follows.

$$G_{QPI}(s) = K_p + \frac{K_r \omega_c}{s + \omega_c} \tag{8}$$

where K_p and K_r are the proportion and integral coefficients of QPI regulator, respectively, and ω_c is the cutoff frequency.

As shown in Fig.2 (b), E_p, E_q can be equivalent to E_α, E_β after transforming E_p, E_q from the *d-q* rotating coordinate frame into the α-β stationary coordinate. Where E_α and E_β are the errors between i_α, i_β and their corresponding references, respectively. Also E_α is the actual current error between the grid-current i_g and its equivalent reference i_{ref} in the actual grid-current control.

So, u_α, u_β can be expressed as follows.

$$\begin{bmatrix} u_\alpha(s) \\ u_\beta(s) \end{bmatrix} = \frac{1}{2}\begin{bmatrix} G_{\mathrm{QPI}}(s+j\omega_0)+G_{\mathrm{QPI}}(s-j\omega_0) & -j[G_{\mathrm{QPI}}(s+j\omega_0)-G_{\mathrm{QPI}}(s-j\omega_0)] \\ j[G_{\mathrm{QPI}}(s+j\omega_0)-G_{\mathrm{QPI}}(s-j\omega_0)] & G_{\mathrm{QPI}}(s+j\omega_0)+G_{\mathrm{QPI}}(s-j\omega_0) \end{bmatrix}\begin{bmatrix} E_\alpha(s) \\ E_\beta(s) \end{bmatrix}$$
$$= \begin{bmatrix} K_\mathrm{p}+\dfrac{K_\mathrm{r}\omega_\mathrm{c}(s+\omega_\mathrm{c})}{s^2+2\omega_\mathrm{c}s+(\omega_0^2+\omega_\mathrm{c}^2)} & -\dfrac{K_\mathrm{r}\omega_\mathrm{c}\omega_0}{s^2+2\omega_\mathrm{c}s+(\omega_0^2+\omega_\mathrm{c}^2)} \\ \dfrac{K_\mathrm{r}\omega_\mathrm{c}\omega_0}{s^2+2\omega_\mathrm{c}s+(\omega_0^2+\omega_\mathrm{c}^2)} & K_\mathrm{p}+\dfrac{K_\mathrm{r}\omega_\mathrm{c}(s+\omega_\mathrm{c})}{s^2+2\omega_\mathrm{c}s+(\omega_0^2+\omega_\mathrm{c}^2)} \end{bmatrix}\begin{bmatrix} E_\alpha(s) \\ E_\beta(s) \end{bmatrix} \tag{9}$$

By substituting equation $E_\beta(s)=(-s/\omega_0)E_\alpha(s)$ into Eq.(9), the transfer function $G_{\mathrm{QPI}}(s)$ is equivalent as Eq.(10) in the α-β stationary coordinate, and $G_{\mathrm{eq}}(s)$ is the proposed SRFQPI controller.

$$G_{\mathrm{eq}}(s)=\frac{u_\alpha(s)}{E_\alpha(s)}=K_\mathrm{p}+\frac{2K_\mathrm{r}\omega_\mathrm{c}(s+0.5\omega_\mathrm{c})}{s^2+2\omega_\mathrm{c}s+(\omega_0^2+\omega_\mathrm{c}^2)} \tag{10}$$

The bode diagram of $G_{\mathrm{eq}}(s)$ is depicted in Fig.3 (a). Compared with the traditional SRFPI controller, the proposed SPRQPI controller not only keeps high gain but also reduces the effect of fundamental frequency offset, which increases the system robustness against the fundamental-frequency variation. The parameters of SRFQPI are designed carefully in section 3.1 and 3.3.

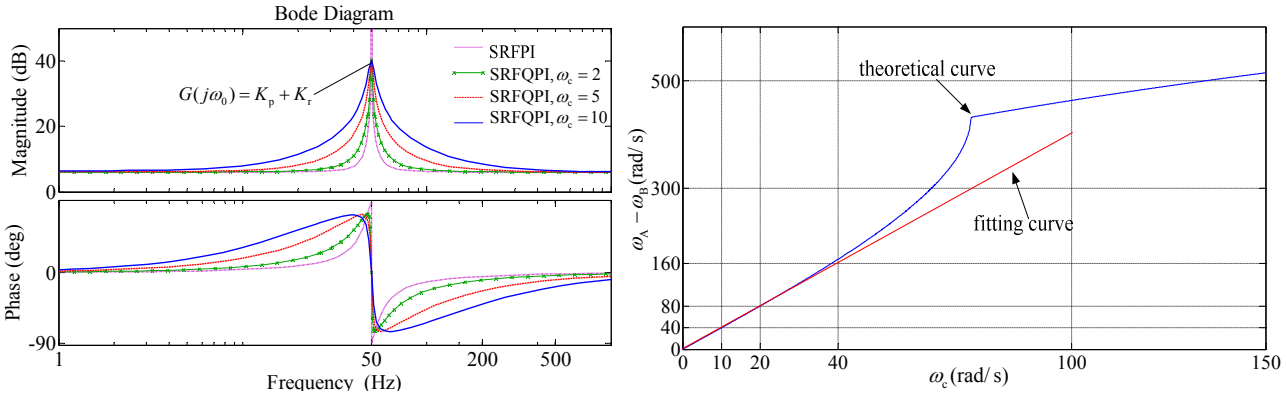

(a) (b)

Fig.3. Bode diagram of the proposed SRFQPI method and the parameter ω_c selecting. (a) Bode diagram (K_p=2, K_r=100, ω_0=100π). (b) The relationship curve between the bandwidth (ω_A-ω_B) and ω_c.

2.2. RGCFAD Controller

The essential cause of the poor robustness to the grid-impedance variation is that the critical frequency of VEDR is located at the LCL-resonance frequency range ($10\omega_0/2\pi$, $0.5f_s$), and the actual LCL-resonant frequency f_r might cross over the critical frequency along with the grid-impedance variation. Hence, in order to improve the system robustness against the wide-range variation of grid-impedance, the RGCFAD controller is proposed to make the VEDR positive in the range (0, $0.5f_s$), as shown in Fig. 2(a). And its transfer function $H(s)$ is expressed as follows.

$$H(s)=-\frac{2K_\mathrm{g}s}{(1+e^{-sT_\mathrm{s}})(s+\omega_\mathrm{g})} \tag{11}$$

where K_g and ω_g are the gain and cut-off angular frequency of RGCFAD controller separately.

So, the transfer function $G_{AD}(s)$ of the active damping loop is expressed as follows.

$$G_{AD}(s)=\frac{i_g(s)}{u_\alpha(s)}=\frac{K_{inv}G_{LCL}(s)G_h(s)/T_s}{1+H(s)K_{inv}G_{LCL}(s)G_{control2}(s)} \tag{12}$$

From Eq. (12), the essence of $H(s)$ is the phase-ahead negative feedback control nearby the actual LCL-resonance frequency. And the deeper the feedback, the better suppression of the LCL-resonance peak is obtained. Since the gain of transfer function $G_{LCL}(s)$ nearby the f_r is negative, $H(s)$ should provide a phase difference 180° to realize the negative feedback control. Meanwhile, the phase-ahead control part can further reduce the serious phase-leg introducing by the control delay $G_{control2}(s)$, and broaden the positive range of VEDR for improving the system robustness against the grid-impedance variation.

In the RGCFAD controller, it is equivalent to the virtual impedance Z_{eq} connected in the middle of the inductance L_2 and grid inductance, as shown in Fig.2 (c). Considering the parasitic resistances R_1 and R_2 enough small to be ignored, the expression of Z_{eq} can be derived as follows.

$$Z_{eq}=-\frac{H(s)G_{control2}(s)K_{inv}}{s^2L_1C} \tag{13}$$

Here, Z_{eq} can be defined as the resistance R_{g1} connected in series with the reactance X_{eq}, and be rewritten as

$$Z_{eq}(\omega)=R_{eq}(\omega)+jX_{eq}(\omega) \tag{14}$$

where $R_{eq}(\omega)$ and $X_{eq}(\omega)$ are easily figured out as follows.

$$\begin{cases} R_{eq}(\omega)=\dfrac{2K_gK_{inv}\sin(0.5\omega T_s)A_1(\omega)}{\omega^2T_sL_1C(\omega^2+\omega_g^2)\cos(0.5\omega T_s)} \\ X_{eq}(\omega)=\dfrac{2K_gK_{inv}\sin(0.5\omega T_s)B_1(\omega)}{\omega^2T_sL_1C(\omega^2+\omega_g^2)\cos(0.5\omega T_s)} \end{cases} \tag{15}$$

where,

$$\begin{cases} A_1(\omega)=\omega\cos 0.5\omega T_s+\omega_g\sin 0.5\omega T_s \\ B_1(\omega)=\omega_g\cos 0.5\omega T_s-\omega\sin 0.5\omega T_s \end{cases} \tag{16}$$

Meanwhile, combined Fig. 2 (c) with Eq. (15), f_r can be rewritten as Eq. (17).

$$f_r=\frac{1}{2\pi}\sqrt{\frac{L_1+(L_2+L_g+X_{eq}/\omega)}{L_1(L_2+L_g+X_{eq}/\omega)C}} \tag{17}$$

According to Eq.(15), the frequency characteristics of $R_{eq}(\omega)$ and $X_{eq}(\omega)$ are depicted in Fig.4 (a), where f_s is the switching frequency, and f_R is the positive or negative critical frequency of equivalent resistance part $R_{eq}(\omega)$, and f_{X1} and f_{X2} are the capacitive or inductive critical frequency of equivalent reactance part $X_{eq}(\omega)$.

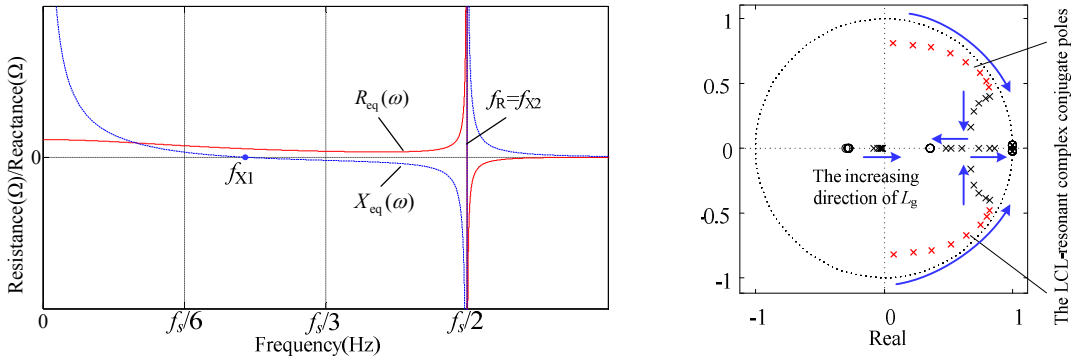

(a) (b)

Fig.4.The feature of the proposed RGCFAD method. (a) Frequency-domain characteristics of R_{eq} and X_{eq}. (b) Closed-loop pole maps with grid-impedance variation.

As shown in Fig.4 (a), the critical frequency of R_{eq} is located outside the LCL-resonance frequency range, and R_{eq} presents positive resistance characteristic in the interval of (0, 0.5f_s) all along. Furthermore, since f_R=f_{X2}, the actual LCL-resonant frequency f_r cannot cross over the f_R even with a larger K_g or a smaller ω_g according to Eq. (17). As a consequence, the RGCFAD method not only eliminates the possibility where the critical frequency of VEDR crosses over the f_r, but also broadens the range of K_g and ω_g, respectively.

Meanwhile, the close-loop transfer function $T_{cl}(s)$ of RTDOF-SCC is expressed as follows.

$$T_{cl}(s)=\frac{K_{inv}G_{LCL}(s)G_{eq}(s)G_{control1}(s)}{1+K_{inv}G_{LCL}(s)[G_{eq}(s)G_{control1}(s)+H(s)G_{control2}(s)]} \tag{18}$$

According to Eq.(18), the closed-loop pole maps of $T_{cl}(s)$ along with grid-impedance variation is shown in Fig.4 (b). Due to the implement of double-sampling mode and RGCFAD method, the LCL-resonant complex conjugate poles are located inside the unit circle all along regardless of the grid-impedance variation. In this case, the LCL-type grid-connected inverter would keep remained stable with wide-range variation of grid-impedance.

3. THE SYSTEM PERFORMANCE ANALYSIS AND OPTIMIZED RTDOF-SCC PARAMETERS DESIGN

In this section, the overall system performance is analyzed in detail, and the optimized parameters of RTDOF-SCC are selected.

To obtain a more intuitive sense, $G_{control2}(s)/(1+e^{-sT_s})$ is rewritten in the frequency domain.

$$\frac{G_{control2}(j\omega)}{1+e^{-j\omega T_s}}=e^{-0.5sT_s}\cdot\frac{j\sin(0.5\omega T_s)}{j0.5\omega T_s}\cdot\frac{1}{2\cos(0.5\omega T_s)}\approx\frac{e^{-0.5j\omega T_s}}{2\cos(0.5\omega T_s)}\approx 0.5 \tag{19}$$

Then, the loop gain $T_o(s)$ of RTDOG-SCC is equivalent as follows.

$$T_o(s) \approx \frac{K_{inv}(s+\omega_g)G_{eq}(s)G_{control1}(s)}{L_1\left(L_2+L_g\right)Cs\left[s^3+\omega_g s^2+\omega_{res}^2 s+\omega_g\omega_{res}^2-\frac{K_g K_{inv}}{L_1\left(L_2+L_g\right)C}\right]} \tag{20}$$

3.1 The bandwidth of SRFQPI analysis and the selecting of ω_c

To improve the system robustness against the variation of ω_0, the bandwidth of SRFQPI should include the variation range of ω_0, as shown in Fig.3 (a). And LCL-filter can be simplified as a simple inductance $s(L_1+L_2)$ to analyze the performance at the low-frequency domain. Then, $T_o(j\omega)$ is simplified as follows.

$$T_o(j\omega) \approx \frac{K_{inv}}{j\omega(L_1+L_2)} \frac{2K_r\omega_c(j\omega+0.5\omega_c)}{2j\omega_c\omega+(\omega_0^2+\omega_c^2-\omega^2)} \tag{21}$$

At the fundamental frequency, the maximum gain of $T_o(j\omega)$ is expressed as $\left|T_o(j\omega)\right|_{max} = K_{inv}K_r / \omega_0(L+L_g)$. According to the definition of the bandwidth, while $\left|T_o(j\omega)\right| = K_{inv}K_r / \sqrt{2}\omega_0(L+L_g)$, the bandwidth of the SRFQPI controller can be figured out as follows.

$$(\omega^2)^2 - 2(\omega_0^2+\omega_c^2)\omega^2 + \omega_0^4 + \omega_c^4 - 6\omega_0^2\omega_c^2 = 0 \tag{22}$$

Solving Eq. (22), it yields

$$\begin{cases} \omega_A^2 = \omega_0^2 - \omega_c^2 + 4\omega_c\omega_0 \\ \omega_B^2 = \omega_0^2 - \omega_c^2 - 4\omega_c\omega_0 \end{cases} \tag{23}$$

Then, the bandwidth of the SRFQPI controller can be obtained and expressed as

$$\omega_A - \omega_B = \sqrt{\omega_0^2 - \omega_c^2 + 4\omega_c\omega_0} - \sqrt{\omega_0^2 - 2\omega_c^2 - 4\omega_c\omega_0} \tag{24}$$

To select the proper ω_c, the theoretical curve between the bandwidth (ω_A-ω_B) and ω_c is depicted in Fig.3 (b), and the fitting curve is also shown by the linearization. Obviously, the slope of the fitting curve is 4, and the bandwidth is approximately $\omega_c/4$. Generally, the frequency fluctuation range at fundamental frequency is ± 0.5 Hz, so $\omega_c = 4$ is selected.

3.2 Optimized parameters design of the RGCFAD controller

From Eq. (20), the generalized open-loop transfer function with ω_g is derived as follows.

$$G_{open}(s) = \frac{\omega_g[L_1(L_2+L_g)Cs^3 + (L_1+L_2+L_g)s + K_{inv}G_{eq}(s)]}{L_1(L_2+L_g)Cs^4 + (L_1+L_2+L_g)s^2 + [G_{eq}(s)-K_g]K_{inv}s} \tag{25}$$

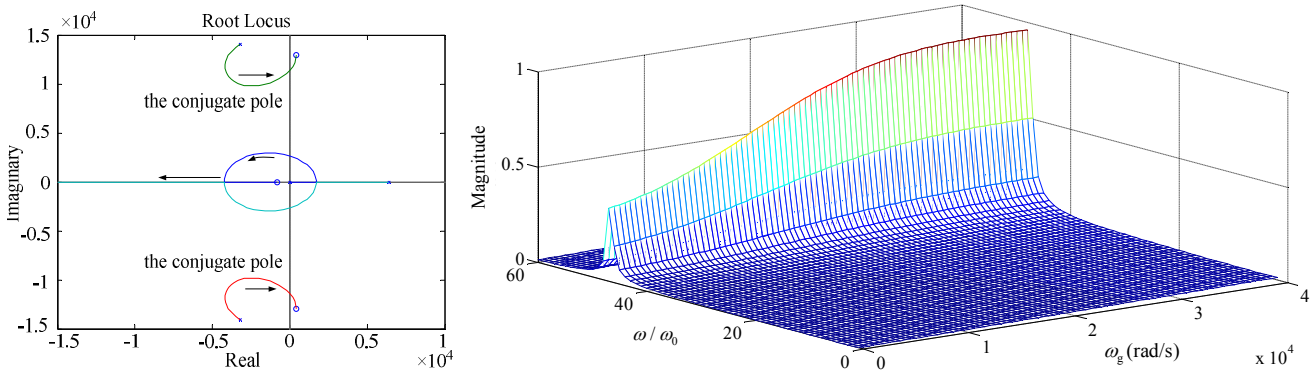

(a) (b)

Fig. 5. Root locus and resonance damp diagram of the proposed control system with ω_g changing. (a) The generalized open-loop root locus of $T_o(s)$ with the gain of ω_g. (b) LCL-resonance suppression with the change of ω_g.

The generalized open-loop root locus with the gain of ω_g is shown in Fig.5 (a), where $G_{eq}(s)$ is simplified as K_p, and K_g=18. With the increase of ω_g, the conjugate poles become the dominant poles gradually, and the dynamic response tends to be worse. As shown in Fig. 5(b), ω_g has a negative correlation with the LCL-resonance suppression. And the smaller ω_g, the LCL-resonance damping is bigger. So, the dynamic performance may achieve the best point when ω_g values its minimum.

From Eq. (20), the characteristic root equation of the transfer function $T_o(s)$ is expressed as:

$$D(s) \approx L_1(L_2+L_g)C[s^3+\omega_{res}^2\omega_g s^3+s^2+\omega_{res}^2\omega_g s-K_g K_{inv}s / L_1(L_2+L_g)C][s^2+2\omega_c s+(\omega_0^2+\omega_c^2)] \tag{26}$$

The above characteristic equation can be also rewritten as the poles mode, given by:

$$D(s) = L_1(L_2+L_g)Cs(s+K_1\omega_n)(s^2+2\xi\omega_n s+\omega_n^2)[s^2+2\omega_c s+(\omega_0^2+\omega_c^2)] \tag{27}$$

where ξ is the damping factor of the conjugate poles, ω_n is the resonant angular frequency of the conjugate poles and its value is approximately equal to $2\pi f_r$, and K_1 is the ratio between the distance from the introduced poles to the imaginary axis and the distance from the complex conjugate poles to the imaginary axis.

Comparing Eq.(26) with Eq.(27), the active damping parameters (ω_g, K_g) and system performance are decided by (ζ, K_1, ω_n). Meanwhile, since the coefficients of Eq.(26) are equal to Eq.(27), the relationships between (ω_g, K_g) and (ζ, K_1, ω_n) can be derived as follows.

$$\begin{cases} \omega_n = \sqrt{1/(2K_1\xi+1)}\,\omega_{res} \\ \omega_g = (K_1+2\xi)\omega_n \\ K_g = [(L+L_g)\omega_g - K_1\omega_n^3 LL_g C]/K_{inv} \end{cases} \tag{28}$$

Referring to the 1st equation in Eq. (28), $K_1\xi$ is constant while ω_n and ω_{res} are assumed as constant. Then, the 2nd equation in Eq.(28) is rewritten as follows.

$$\omega_g = (\sqrt{\frac{K_1}{\xi}} + 2/\sqrt{\frac{K_1}{\xi}})\sqrt{K_1\xi/(2K_1\xi+1)}\omega_{res} \tag{29}$$

Obviously, ω_g only depends on the K_1/ξ. While $K_1=2\xi$, ω_g obtains the minimum value.

The bode diagram of $T_o(s)$ is depicted in Fig. 6. The value of K_1/ξ is set to 0.2, 0.5, 2, 4 and 10, respectively, and ω_n is 1.55×10^4rad/s. In order to analyze the system performance, referring to Eq.(25) and Fig.6, K_1/ξ can be considered in two cases: (i) When $K_1<2\zeta$, no resonance peak exists. However, with the decreasing K_1/ζ, the stability margin becomes worse. (ii) When $K_1\geq2\zeta$, with the K_1/ζ increasing, the stability margin gradually turns better. However, compared with $K_1/\xi=2$, a poorer LCL-resonance suppression and dynamic performance are yielded. Hence, the reasonable value of K_1/ξ should be 2, where a balance among the LCL-resonance damping, the stability margin and the dynamic performance is achieved.

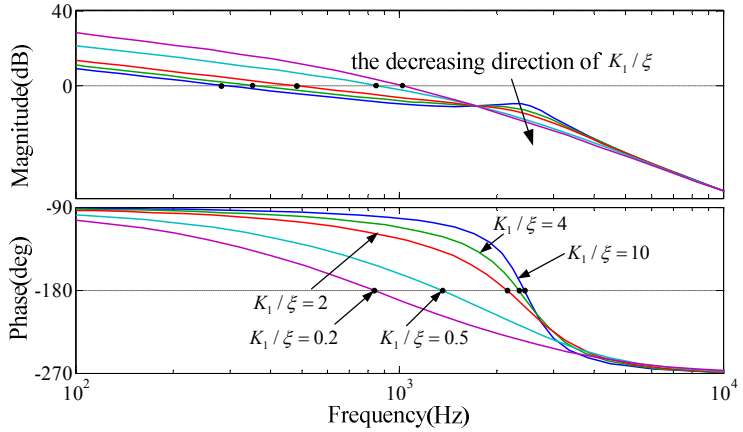

Fig.6. Bode diagram of $T_0(s)$ with the different ratio between K_1 and ζ (K_p=1, K_r=0).

Then, substituting $K_1=2\xi$ into Eq. (28), the two parameters of active damping loop are simplified as follows.

$$\begin{cases} \omega_g = 4\sqrt{\xi^2/(4\xi^2+1)}\omega_{res} \\ K_g = \dfrac{2\xi(L+L_g)}{K_{inv}\sqrt{4\xi^2+1}}\omega_{res}[2-\dfrac{1}{4\xi^2+1}] \end{cases} \tag{30}$$

Obviously, the values of ω_g and K_g only depend on ζ alone. As a result, the system could obtain the optimal operating condition only by regulating ζ, and the complexity of parameters (ω_g, K_g) design is also significantly reduced.

3.3 The system stability analysis and the selecting of parameters ζ, K_p and K_r

Since the cutoff frequency ω_{sc} and ω_n are higher than the fundamental frequency, $G_{eq}(s)$ can be simplified as $G_{eq}(s)=K_p$ to calculate the gain margin (GM) and phase margin (PM) of the open loop $T_o(s)$ at ω_{sc} and ω_n. Based on the abovementioned optimized design of the RGCFAD controller, the GM and PM of overall system can be easily derived as follows.

$$\begin{cases} GM = 20\lg\left|T_0(j\omega_{sc})\right| - 20\lg\left|T_0(j\omega_n)\right| = 20\lg\left|\dfrac{2\xi\sqrt{\xi^2\left(64\xi^2+6\right)^2+\left(8\xi^2+1\right)^2}}{\dfrac{\omega_{sc}}{\omega_{res}}(4\xi^2+1)^{3/2}(16\xi^2+1)(2-\dfrac{\omega_{sc}^2}{\omega_{res}^2}-\dfrac{1}{8\xi^2+2})}\right| \\ PM = \angle T_0(j\omega_{sc}) + 180^\circ = \arctan\dfrac{K_p\omega_{sc}}{K_r\omega_c} + \arctan\dfrac{\sqrt{1+4\xi^2}\,\omega_{sc}}{4\xi\omega_{res}} - \arctan\dfrac{\sqrt{1+4\xi^2}\,\omega_{sc}}{2\xi\omega_{res}} - \arctan\dfrac{2\xi\sqrt{1+4\xi^2}\,\dfrac{\omega_{sc}}{\omega_{res}}}{1-(4\xi^2+1)\dfrac{\omega_{sc}^2}{\omega_{res}^2}} \end{cases} \tag{31}$$

Seen from Eq. (31), ξ and ω_{sc}/ω_{res} affect both the GM and PM, and K_p and K_r only affect the PM. In generally, to guarantee a fast dynamic response and good ability of attenuating high-frequency harmonic currents, ω_{sc} is set to $1/10f_s$ [15]. In this case, ω_{sc}/ω_{res} is 0.27. And according to $|T_o(j\omega_{sc})|=1$, K_p can be derived as follows.

$$K_p = \omega_{sc}\left(L+L_g\right)\left[2-\frac{\omega_{sc}^2}{\omega_{res}^2}-\frac{1}{8\xi^2+2}\right]/K_{inv} \tag{32}$$

So, the GM is only determined by ξ, and the PM is determined by ξ and K_r.

The relations between the parameter ξ and GM, PM are depicted in Fig. 7 (a) and (b), respectively. To obtain the proper stability margin, GM≥3dB and PM≥45° are required. As shown in Fig.7 (a), to keep the GM is above 3dB, it needs $\xi>\xi_{min}$, where ξ_{min} is the intersection point between the GM curve and the standard curve of 3dB. Seen from Fig.7 (b), to keep the PM be above 45°, it needs $\xi<\xi_{max}$, where ξ_{max} is the intersection point between the PM curve and the standard curve of 45°. But ξ_{max} varies with K_r, and ξ_{max} constantly reduces with the increasing K_r. Once ξ_{max} is smaller than ξ_{min}, ξ has no value to satisfy GM≥3dB and PM≥45° simultaneously. For instance, while K_r=600 or 900, the PM cannot obtain the value higher than 45°regardless of ξ selecting any value. So, K_r cannot select to be too large value, and must satisfy the follow condition in Eq. (33).

$$K_r \le \frac{\omega_{sc}^2\left(L_1+L_2\right)\left(2-\dfrac{\omega_{sc}^2}{\omega_{res}^2}-\dfrac{1}{8\xi_{min}^2+2}\right)}{K_{inv}\tan\left(\dfrac{\pi}{4}+\arctan\dfrac{\sqrt{1+4\xi_{min}^2}\,\omega_{sc}}{2\xi_{min}\omega_{res}}+\arctan\dfrac{2\xi\sqrt{1+4\xi_{min}^2}\,\dfrac{\omega_{sc}}{\omega_{res}}}{1-(4\xi_{min}^2+1)\dfrac{\omega_{sc}^2}{\omega_{res}^2}}-\arctan\dfrac{\sqrt{1+4\xi_{min}^2}\,\omega_{sc}}{4\xi_{min}^2\omega_{res}}\right)\omega_c} \tag{33}$$

Meanwhile, in order to meet the grid-current amplitude error (i_{ref} -i_g) less than 1%, $|T(j\omega_0)|\approx K_{inv}K_r/\omega_0(L_1+L_2)$ should satisfy the following condition.

$$\left|\frac{T(j\omega_0)}{1+T(j\omega_0)}\right| \ge 0.99 \tag{34}$$

Solving Eq. (34), it yields

$$K_r \ge 99\omega_0(L_1+L_2)/K_{inv} \tag{35}$$

According to Eq. (33) and Eq. (35), the interval of K_r can be easily acquired. Once K_r is determined, ξ is located within the interval of (ξ_{min}, ξ_{max}).

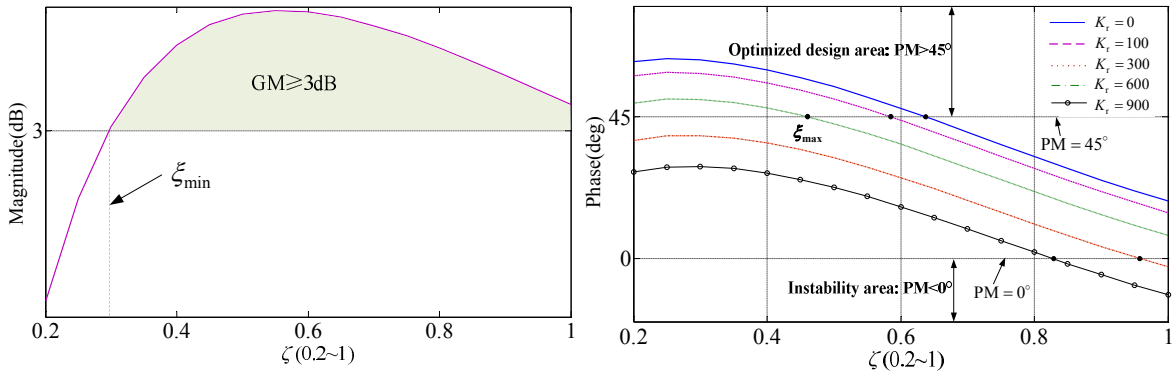

(a) (b)

Fig.7. The PM and GM of the open loop with ξ. changing. (a) The relationship between GM and ξ. (b) The relationship between PM and ξ.

4. SIMULATION AND EXPERIMENT RESULTS

4.1 Simulation results

The simulation is established by Matlab/Simulink, and simulation parameters of PV system are listed in Tab. 1. The ambient temperature is set to 25 ℃, and the standard light intensity is set to 1000 W/m^2.

Tab.1
The simulation parameters of PV system

parameter	Value	parameter	Value
P/kW	2.2kW	u_s/V	220
ω_0/(rad/s)	2π×50	L_b/mH	2.8
L_1/mH	0.7	U_{dc}/V	400
L_2/mH	0.4	C_{dc}/μF	3600
C/μF	10	r_1/Ω	0.16
T_s/s	1/10000	r_2/Ω	0.09
ω_c/(rad/s)	4	K_{pwm}	1
ω_{res}/(10^4rad/s)	1.98		

To verify the optimal operation point ($K_1/\xi = 2$), Fig.8 (a), (b) and (c) show the waveforms when the light intensity increasing from 500 W/m^2 to 1000 W/m^2 under the different ratios of K_1/ζ, where $\omega_n = 0.8\omega_{res}$, K_p=2, K_r=250, and a disturbance signal with 16900rad/s is introduced. While K_1/ξ=0.3, the THD of grid-current is up to 70.82%, and the PV system is instability, as shown in Fig.8 (a). While K_1/ξ=10, the THD of grid current is only 1.13%, but the PV system yields a resonance peak around the LCL-resonance frequency, as shown in Fig. 8 (c). While $K_1/\xi = 2$, the THD of grid current is only 0.47%, and the resonance peak is greatly suppressed, as shown in Fig. 8 (b). Meanwhile, the overshoot of grid current is only 15% and the PV system has a faster

dynamic response than other conditions. In summary, the system obtains the optimal operation point with the condition of $K_1/\xi =$ 2.

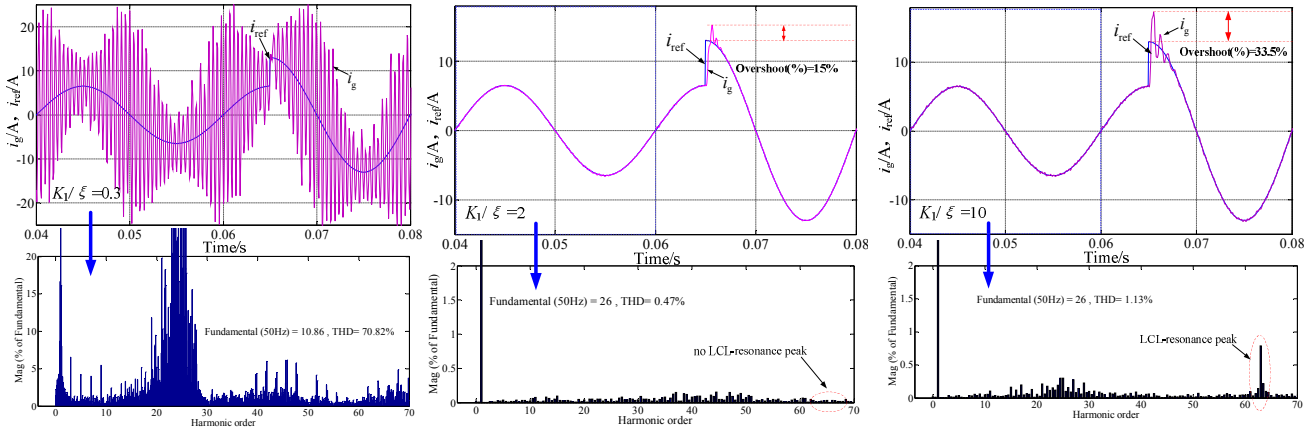

(a) (b) (c)

Fig.8. Dynamic simulation results of grid current with the proposed RTDOF-SCC under different ratios of K_1/ξ. (a) K_1/ξ=0.3. (b) K_1/ξ=2. (c) K_1/ξ=10.

To select the proper parameters for RTDOF-SCC method, ξ_{min} should be higher than 0.3 to satisfy GM≥3dB based on Eq. (31) and LCL-filter parameters in Tab.1. Then, the interval of K_r is easily selected ranging from 35 to 828 according to Eq.(33) and Eq.(35). To satisfy PM≥45°and a smaller amplitude error, K_r is selected as 300, and ξ_{max} is easily selected as 0.4 according to Fig.7 (b). And K_p is selected as 1.78 according to Eq.(32). Finally, the control parameters of RTDOF-SCC method are selected without complicated trial as shown in Tab.2. In this case, PM and GM of the PV system are 47.7° and 4.4dB, respectively, and the LCL-type grid-connected PV system can obtain a good stability.

Tab.2
The control parameters of the RTDOF-SCC method

parameter	Value	parameter	Value
ω_c/(rad/s)	4	ω_{sc}/(10^3rad/s)	6.28
K_p	1.78	ω_g/(10^4rad/s)	2.48
K_r	300	ω_n/(10^4rad/s)	1.55
K_g	18.9	ω_{res}/(10^4rad/s)	1.98
ζ	0.4		

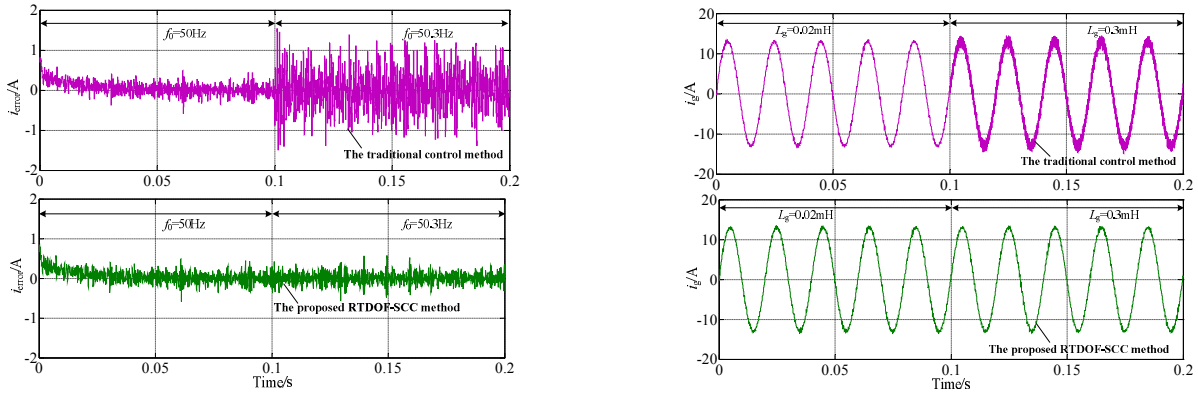

(a) (b)

Fig.9. Comparative simulation results of the grid-current amplitude error and grid current under the different control methods. (a) The grid-current amplitude error i_{error} with the grid-frequency variation. (b) The grid current with the grid-impedance variation.

To verify the effectiveness of proposed RTDOF-SCC method, comparative simulation results with the grid-frequency variation and grid-impedance variation are shown in Fig.9 (a)-(b), respectively. Where the grid-current amplitude error i_{error} is defined as (i_g-i_{ref}); the traditional single-current control (SCC) method is defined as the SRFPI and GCF active damping method with HPF.

As shown in Fig.9 (a), when the grid frequency changes from 50Hz to 50.3Hz, the grid-current amplitude error instantly increases from 0.17A to 0.63A under the traditional single-current method, but the proposed RTDOF-SCC method can still track the reference grid-current with smaller amplitude error regardless of the grid-frequency variation. Compared with the traditional single-current control method, the RTDOF-SCC method enhances the system adaptability against grid-frequency fluctuation.

As shown in Fig.9 (b), at t=0s, a disturbance signal 16900rad/s is introduced, and at t=0.1s, the grid impedance varies from 0.02mH to 0.3mH. Using the traditional single-current method, the waveform of grid current appears oscillation while L_g=0.3mH, because the VEDR of GCF active damping with HPF is approximately equal to 0. But with the implement of RTDOF-SCC method, the waveform always remains smooth regardless of the grid-impedance variation. The RTDOF-SCC method also obviously improves the system robustness against the grid impedance variation.

4.2 Experiment results

The 2.2-kW laboratory LCL-type grid-connected PV system is built, which is composed of the building PV arrays, dc/dc converter, full-bridge inverter, DSP control system, and etc. IPM Module (PM505LA060) is chosen as the power switch device. TMS320F2812 and AD7656 are used as the controller and sampling chip, respectively. The parameters of PV system are shown in Tab.1 and Tab.2. The steady-state experimental results are shown in Fig. 10 and Fig.11 by a power quality analyzer FLUKE43B, and the dynamic experimental results are show in Fig.11 by the digital high-speed oscilloscope TPS 2024 (Tektronix).

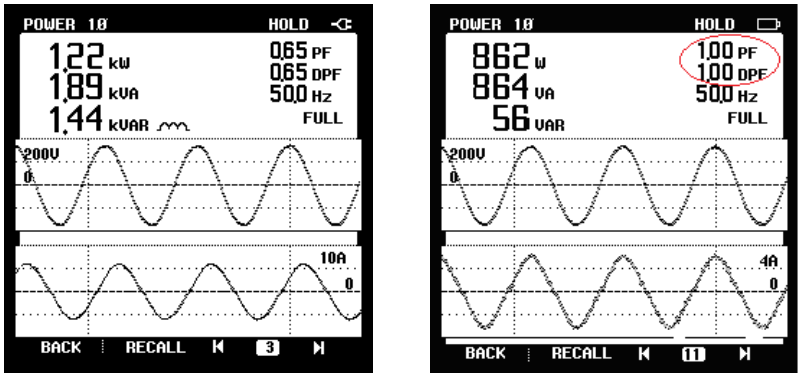

(a) (b)

Fig.10 Experimental results of the currents and output power waveforms with the proposed RTDOF-SCC method under the resistor-inductance loads condition. (a) The grid-current i_g and inverter output power. (b) The true injected grid-current i_s and injected grid power.

Fig.10 (a) and (b) show the experimental results of the grid current and output power with the RTDOF-SCC method under the resistor-inductance loads condition. Obviously, the grid-connected inverter transfers PV energy into the grid and the local loads, and the grid power factor (PF) is close to 100%. The proposed RTDOF-SCC method not only provides active power and feeds the redundant energy into the grid quickly, but also regulates the reactive power to realize the reactive compensation.

Fig.11 (a) and (b) show the comparative results of the grid-current THD under the different control methods while the grid frequency shifts. Compared with the traditional single-current method, the RTDOF-SCC method can track accurately the PV energy and enhance further the system performance.

Fig.11 (c)~(f) show the comparative waveforms of the grid current with grid-impedance variation under the different control methods. Using the traditional single-current control method, the actual resonance frequency is more close to the critical frequency of VEDR while L_g=0.3mH, and the system tends to oscillate and become unstable, as shown in Fig. 11 (c) and (d). However, while the proposed method is applied, the VEDR shows positive characteristic at the actual resonant frequency, and the grid current becomes smooth and tracks accurately the reference current, as shown in Fig. 11(e) and (f). The system is also tested with the different grid impedance ranging from 0.5 mH to 3.0 mH, and the THD of i_g always remains below 3.2%. The proposed method greatly enhances the system robustness against the grid-impedance variation.

Fig. 11 (g)~(h) show the dynamic waveforms of the PV system when the load suddenly changes from half to full power under the different control methods. As a result, the proposed method has a faster dynamic response, and smaller overshoot compared with the traditional single current control method.

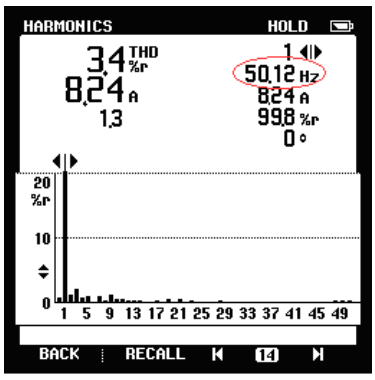

(a)

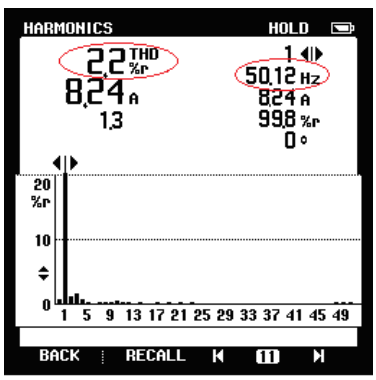

(b)

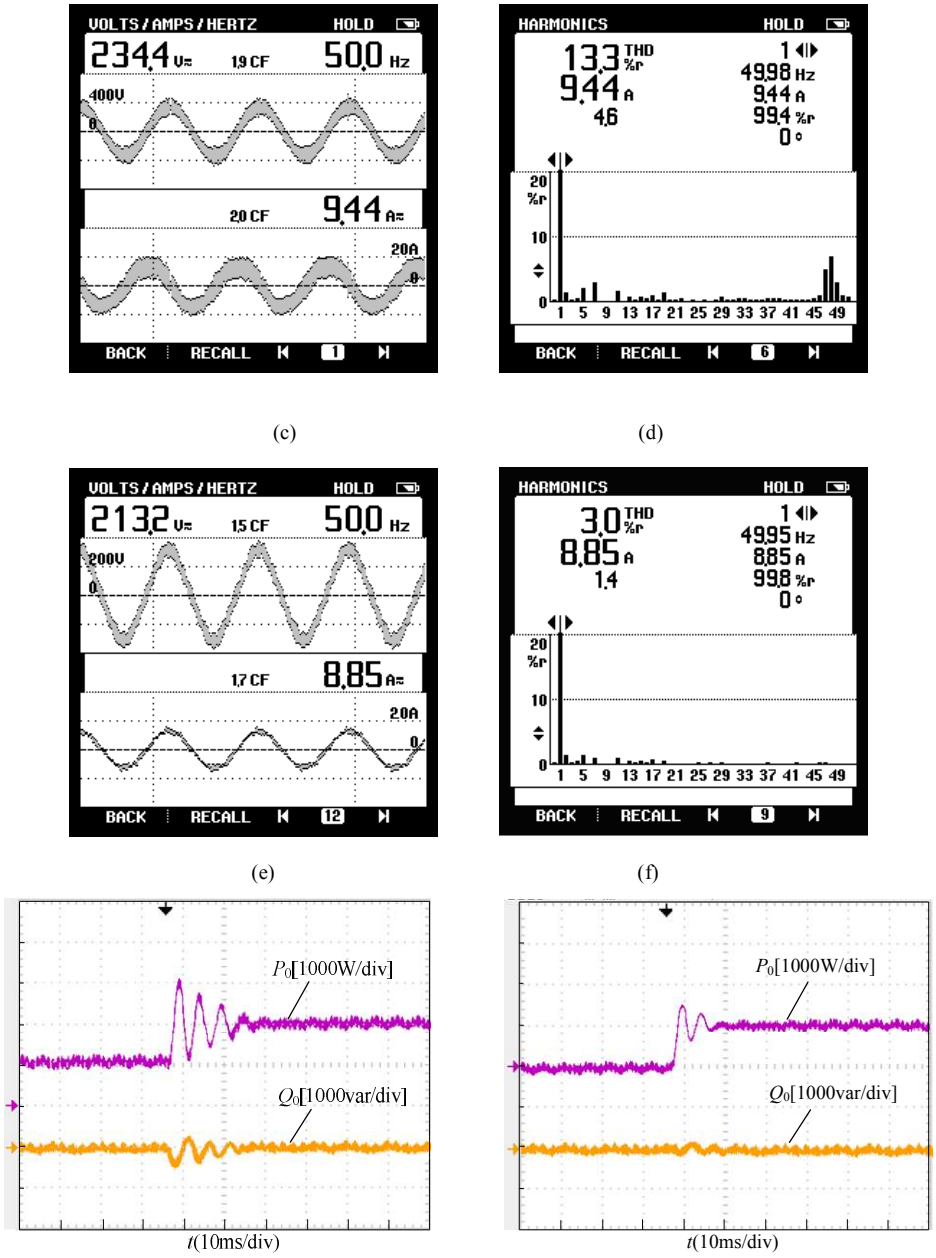

Fig. 11. Comparative experimental results under the different control methods. (a) The THD of grid current under the traditional SCC method with the grid frequency shifting. (b) The THD of grid current under the RTDOF-SCC method with the grid frequency shifting. (c) The waveform of i_g under the traditional SCC method with L_g=0.3mH. (d) The THD of i_g under the traditional SCC method with L_g=0.3mH. (e) The waveform of i_g under the RTDOF-SCC method with L_g=0.3mH. (f) The THD of i_g under the RTDOF-SCC method with L_g=0.3mH. (g) Dynamic waveforms of output powers under the traditional SCC method. (h) Dynamic waveforms of output powers with the RTDOF-SCC method.

5 CONCLUSIONS

For single-phase LCL-type grid-connected DGs installed at the end of the grid, a RTDOF-SCC strategy is proposed to improve the system robustness against the grid-frequency fluctuation and grid-impedance variation, which is mainly composed

with SRFQPI and RGCFAD control. The proposed SRFQPI control can compensate reactive power, and regulate the instantaneous grid-current without steady-state error regardless of the fundamental frequency fluctuation. The proposed RGCFAD control damps well the LCL-resonance peak regardless of the grid impedance variation. To realize a good damper, fast dynamic response, and high system stability, the proper parameters of RTDOF-SCC strategy are selected without complicated trial. The performance of RTDOF-SCC strategy is validated by the results from a 2.2-kW laboratory LCL-type grid-connected PV system. Moreover, the proposed method can be also applied commercially to the microgrid.

6 ACKNOWLEDGEMENTS

This work was supported by the Program of National Natural Science Foundation of China under Grant Number 51237003, 51477045, partially by the Fundamental Research Funds for the Central Universities.

7 REFERENCES

[1] Dos Santos, E.C., Jacobina, C.B., Rocha,N., Dias, J.A.A., Correa, M.B.R.: 'Single-phase to three-phase four-leg converter applied to distributed generation system', *IET Power Electron*., 2010, 3, (6), pp. 892-903

[2] Luo, A., Chen, Y., et al.: 'An Improved Reactive Current Detection and Power Control Method for Single-Phase Photovoltaic Grid-Connected DG System', *IEEE Trans. Energy. Convers*., 28, (4), pp. 823-831

[3] Balasubramanian, A.K., John, V. :'Analysis and design of split-capacitor resistive inductive passive damping for LCL filters in grid-connected inverters', *IET Power Electron*., 2013, 6, (9), pp. 1822-1832

[4] Xu, J., Xie, S., Tang, T.: 'Improve control strategy with grid-voltage feed forward for LCL-filter-based inverter connected to weak grid', *IET Power Electron*., 2014, 7, (10), pp. 2660-2671

[5] Golestan, S., Ramezani, M., et al.: 'dq-frame cascaded delayed signal cancellation-based PLL: analysis, design, and comparison with moving average filter-based PLL', *IEEE trans. Power Electron*., 2015, 30, (3), pp. 1618-1632

[6] Liserre, M., Teodorescu, R., Blaabjerg, F.: 'Stability of photovoltaic and wind turbine grid-connected inverters for a large set of grid impedance values', *IEEE Trans. Power Electron.*, 2006, 21, (1), pp. 263-272.

[7] Akagi H., Watanabe E., Aredes M.,: 'Instantaneous power theory and applications to power conditioning', Wiley-IEEE Press, 2007.

[8] Wu L., Zhao Z., Liu J.,: 'A single-stage three-phase grid-connected photovoltaic system with modified MPPT method and reactive power compensation', *IEEE Trans. Energy. Convers.,* 22, (4), pp. 881-886

[9] Tanaka, T., Hiraki, E., Ueda, K., Sato, K., Fukuma, S.: 'A novel detection method of active and reactive currents in single-phase circuits using the correlation and cross-correlation coefficients and its applications', *IEEE Trans. Power Del.*, 2007, 22, (4), pp. 2450–2456

[10] Monfared, M., Golestan, S., Guerrero, J.M.: 'Analysis, design, and experimental verification of a synchronous reference frame voltage control for single-phase inverters', *IEEE Trans. Ind. Electron.*, 2014, 61, (1), pp. 258-269

[11] Wu, E., Lehn, P. W.: 'Digital current control of a voltage source converter with active damping of LCL resonance', *IEEE Trans. Power Electron.*, 21, (5), pp. 1364–1373

[12] Pan, D., Ruan, X., Bao, C.: 'Capacitor current feedback active damping with reduced computation delay for improving robustness of LCL-type grid-connected inverter', *IEEE Trans. Power Electron*., 2014, 29, (7), pp.3414-3427.

[13] Wu, E., Lehn, P. W.: 'Digital current control of a voltage source converter with active damping of LCL resonance', *IEEE Trans. Power Electron.*, 2006, 21, (5), pp. 1364–1373.

[14] Xu, J., Xie, S., Tang, T.: 'Active damping based control for grid-connected LCL-filtered inverter with injected grid current feedback only', *IEEE Trans. Ind. Electron*, 2014, 61, (9), pp.4746-4758.

[15] Wang, X., Blaabjerg, F., Loh, P.: 'Grid-Current-Feedback Active Damping for LCL Resonance in Grid-Connected Voltage Source Converters', *IEEE Trans. Power Electron.*, 2016, 31, (1), pp. 213-223

[16] Parker, S. G., McGrath, B. P., Holmes, D. G.: 'Regions of active damping control for LCL filters', *IEEE Trans. Ind. Appl.*, 2014, 50, (1), pp. 424-432.

[17] Yang, D., Ruan, X., Wu, H.: 'A real-time computation method with dual sampling mode to improve the current control performance of LCL-Type grid-connected inverter', *IEEE Trans. Ind. Electron*., 2010, 57, (3), pp.954-962

[18] Liserre, M., Teodorescu, R., Blaabjerg, F.: 'Stability of photovoltaic and wind turbine grid-connected inverters for a large set of grid impedance values', *IEEE Trans. Power Electron.*, 2006, 21, (1), pp. 263-272.

[19] Gabe, I. J., Montagner, V. F., Pinheiro, H.: 'Design and implementation of a robust current controller for VSI connected to the grid through an LCL filter', *IEEE Trans. Power Electron.*, 2009, 24, (6), pp. 1444–1452